Distinguishing dynamical quantum criticality through local fidelity distances

Ruchira V. Bhat and Soumya Bera
Department of Physics, Indian Institute of Technology Bombay, Mumbai 400076, India

(Received 3 September 2023; revised 1 May 2024; accepted 13 June 2024; published 26 June 2024)

Using local quantum fidelity distances, we study the dynamical quantum phase transition in integrable and nonintegrable one-dimensional Ising chains. Unlike the Loschmidt amplitude, the standard measure for distinguishing between two quantum states to describe the dynamical quantum phase transition, the local fidelity requires only a part of the system to characterize it. The nonanalyticities in the quantum distance between two subsystem density matrices identify the critical time and the corresponding critical exponent reasonably well in a finite-size system. Moreover, we propose a distance measure from the upper bound of the local quantum fidelity for certain quench protocols where the entanglement entropy features oscillatory growth in time. This local distance encodes the difference between the eigenvalue distribution of the initial and quenched subsystem density matrices and quantifies the critical properties. The alternative distance measure could be employed to examine the dynamical quantum phase transitions in a broader range of models, with implications for gaining insights into the transition from the entanglement perspective.

DOI: 10.1103/PhysRevB.109.214313

I. INTRODUCTION

Conventional symmetry breaking quantum phase transitions are described within the Landau-Ginzburg paradigm, where the free energy density becomes nonanalytic at the transition point [1,2]. Unlike the symmetry breaking quantum phases, the topological phases are understood from the response of the wave function under small adiabatic changes of the Hamiltonian and are characterized by topological invariants [3–5]. In contrast, an out-of-equilibrium phase transition signaled by the nonanalyticities in time, such as the dynamical quantum phase transition (dQPT), is characterized by the zeros of the boundary partition function in the complex time plane [6–9]. The boundary partition function is defined via the Loschmidt amplitude $\mathcal{L}(z) = \langle\psi_0|\, e^{-zH}\, |\psi_0\rangle$, where $z = it$ is the imaginary time, and ψ_0 is the initial state; the nonanalyticities of the boundary partition function translate as the singularities of the rate function,

$$\lambda(t) = -\lim_{L\to\infty} \frac{1}{L} \log |\, \langle\psi_0|\, e^{-iHt}\, |\psi_0\rangle\, |^2, \tag{1}$$

which defines the critical time t^* of such phase transition [6,10–15]. The $\lambda(t)$ obeys dynamical scaling laws in accordance to conventional phase transition and provides the initial framework to analyze, predict, and classify the dQPTs.

For example, the dQPT observed in one-dimensional (1D) integrable and nonintegrable transverse field Ising models (TFIMs) during a global quench between paramagnetic and ferromagnetic phases falls in the Ising universality class, where $\lambda(t)$ follows a power-law scaling in time with an exponent, $\nu \simeq 1$ [10,16]. Conversely, the dQPT in the two-dimensional (2D) Ising model belongs to a different universality class that is characterized by logarithmic scaling of $\lambda(t)$ in time [10]. Moreover, in systems with underlying equilibrium topology, the dQPT is characterized not only by $\lambda(t)$ but also by a dynamical topological order parameter [17–25]. Even though the condition of observing dQPT was initially associated with the presence of an equilibrium critical point [11,26,27], it has now become accepted that dQPTs are fundamentally nonequilibrium phenomena that can occur without any equilibrium counterpart [28–33].

However, relying solely on $\lambda(t)$ and the topological order parameter presents challenges in fully understanding dQPTs, primarily for two reasons. First, these observables fall short in distinguishing dQPTs resulting from distinct quenches that exhibit apparent differences in entanglement entropy and the dynamics of local correlations [34–38]. The entanglement echo, a rate function analog that encodes the deviation of the initial entanglement ground state from the instantaneous value associated with the time evolved entanglement state, partially addresses the above-mentioned issue by distinguishing dQPTs with and without oscillations in the entanglement entropy growth in time [37]. Secondly, global observables are usually challenging to access in generic experiments.

Recently, Jurcevic *et al.* [39] simulated the temporal dynamics of an interacting transverse field Ising model in a finite number of trapped ions. The appearance of dQPT was revealed through the nonanalyticities in the rate function within the degenerate ground state manifold, $\lambda_p(t) = -\min_{p\,\in\,(\uparrow,\downarrow)} \log |\, \langle\psi_p|\, e^{-iHt}\, |\psi_p\rangle\, |^2/L$, where $|\psi_{\uparrow(\downarrow)}\rangle$ is the symmetry breaking doubly degenerate state and in the thermodynamic limit $L \to \infty$ the finite-size $\lambda_p(t)$ converges to the rate function (1). This paper further establishes a direct connection between this microscopic probability and the macroscopic observables by demonstrating a repeated crossover in magnetization dynamics between positive and negative sectors, along with entanglement production near the critical time.

There are also a few theoretical advances in defining local observables to characterize dQPTs. For instance, a real-space local effective free energy [40] and a quasilocal string measure [16,41], have been introduced as local

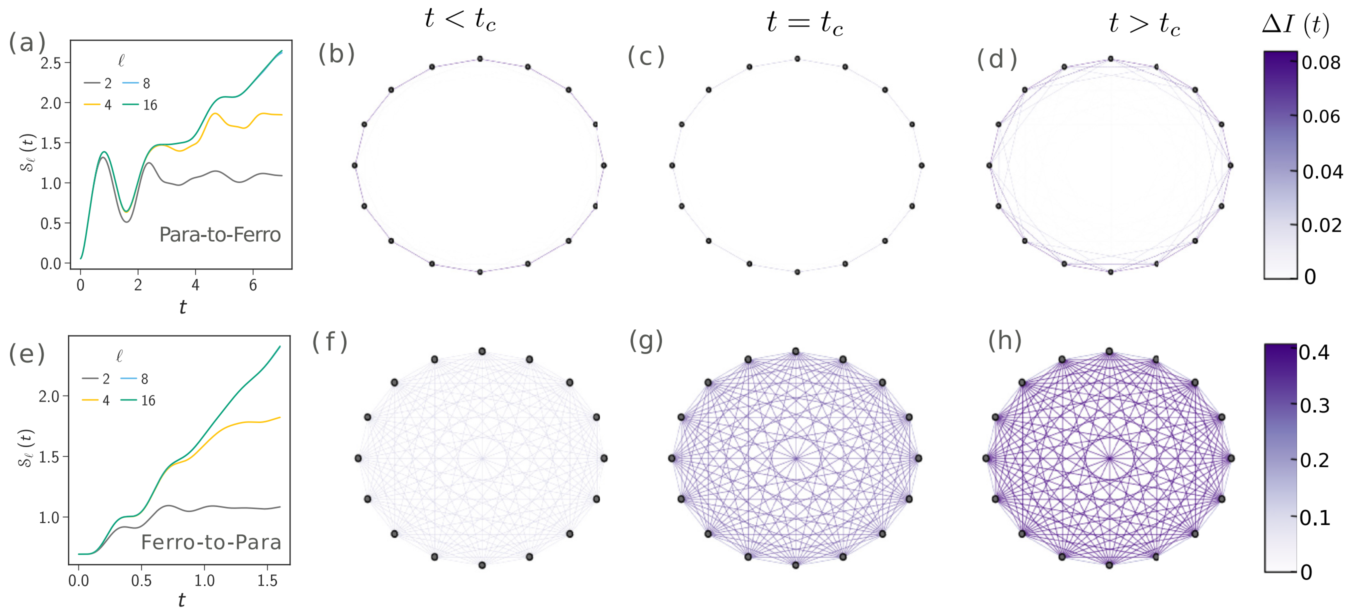

FIG. 1. Entanglement entropy and mutual information for TFIM. (a), (e) Entanglement entropy with oscillatory and nearly linear growth with time under quench I and quench II (see text for the definition of the quench protocols) for the transverse field Ising model, defined in Eq. (6). (b)–(d) Change in mutual information between two spins during quench I at three instants of time, where t_c is the critical time. (f), (h) Mutual information change for the opposite quench. The change in long-range correlations observed for quench II is almost fives times more than that for quench I.

observables to characterize dQPTs. The real-space local effective free energy, $\lambda_M(t) = -\log|\mathcal{L}_M(t)|^2/M$ where $|\mathcal{L}_M(t)|^2 = \langle\psi(t)|\, P_M^z\, |\psi(t)\rangle$, M is the subsystem size in the real space, and $P_M^z = \frac{1}{L}\sum_{i=1}^{L}\frac{1}{2^M}\Pi_i^{i+M}(I_i+\sigma_i^z)$ is the projector, can be thought of as the rate function corresponding to a smaller part of the system, such that in the limit $M \to L$, $\lambda_M(t) \approx \lambda(t)$. Furthermore, the momentum local counterpart of $\lambda_M(t)$, which is calculated in terms of two point single-particle correlations in the integrable limit, facilitates the experimental detection of dQPT, particularly in scenarios where measurement of local observables in k space is involved [16,40]. However, it is not evident whether these local order parameters will be sufficient to distinguish dQPTs with different behavior of entanglement entropy and subsystem correlations in time.

Here, we propose two local quantum distance measures, quantum reduced fidelity distance (qRFD) and minimum reduced fidelity distance (mRFD), to characterize dQPTs observed in integrable and nonintegrable spin models. We investigate two quench protocols that show distinct behaviors in entanglement entropy growth: one showing oscillatory growth and the other exhibiting linear growth near the critical time as shown in Figs. 1(a) and 1(e). The qRFD quantifies the distinguishability between reduced density matrices before and after the quench and displays nonanalytic behavior associated with the corresponding dQPT, regardless of the quench protocol. In contrast, the mRFD differentiates between the eigenvalue distribution of initial and quenched reduced density matrices, characterizing the oscillatory entanglement growth, and therefore the dQPT.

The computation of mRFD requires only the eigenvalues of the reduced density matrices. It implies that for integrable models (with and without nontrivial underlying momentum space topology) the single-particle correlation matrix, which scales with the linear dimension of the system, is sufficient to find the relevant scaling exponents.

II. LOCAL DISTANCE MEASURES

A. Quench protocols

We consider two quench protocols that show dQPT in spin and fermionic chains. The first type, quench I, from the paramagnetic (trivial) to ferromagnetic (topological) phase, shows oscillations [see Fig. 1(a)] in the growth of entanglement entropy at initial times and concomitantly avoided level crossings in the reduced density matrix spectrum near the transition time (see Sec. III A 2 for details). Quench II exhibits a linear increase in entanglement $\mathcal{S}(t) = -\mathbf{Tr}[\rho^\ell(t)\log\rho^\ell(t)]$, where $\rho^\ell(t)$ is the time dependent subsystem ℓ density matrix, as seen in Fig. 1(e) with time, and a gap in the reduced density matrix spectrum. A further differentiation can be made between these two quenches by understanding the spatial entanglement structure after the quench, which we discuss in the following.

Local entanglement correlation

The spatial entanglement structure is fundamentally different depending on the direction of the quench. We quantify these correlations through mutual information $I(A,B) = \mathcal{S}(A) + \mathcal{S}(B) - \mathcal{S}(A\cup B)$, where A and B are two subsystems with $\mathcal{S}(A)$ being the entanglement entropy of subsystem A [42]. Figure 1 shows the change in mutual information between two spins at sites i, j; $\Delta I(t) = I_{i,j}(t) - I_{i,j}(0)$, after quench I [Figs. 1(b)–1(d)] and quench II [Figs. 1(f)–1(h)] at three instants of time.

The emergence of long-range correlations in the ferromagnetic-to-paramagnetic quench, as seen in Figs. 1(f)–1(h), emphasizes the importance of employing measures beyond the local fidelity distance between diagonal reduced density matrices to probe such correlations at longer times. Conversely, when the spatial entanglement remains local, we show that a minimum local distance enables the characterization of dQPTs at finite times for a finite-size system. This approach has practical value, particularly in experimental investigations.

B. Quantum reduced fidelity distance

The Loschmidt amplitude, $\mathcal{L}(t) = \langle\psi_0|\,|\psi(t)\rangle$, which defines the rate function (1), is the quantum fidelity. For a quenched system, the quantum fidelity, $F(t) = [\mathbf{Tr}\sqrt{\sqrt{\rho_0}\rho(t)\sqrt{\rho_0}}]^2$, measures the distinguishability between the initial and quenched state with density matrices ρ_0 and $\rho(t)$ respectively [43,44]. Similar to the rate function, the quantum fidelity is also a global observable that requires access to the entire many-body wave function.

We define a local quantum reduced fidelity for a subsystem size ℓ as

$$F_\ell\big(\rho_0^\ell, \rho^\ell(t)\big) = \left(\mathbf{Tr}\sqrt{\sqrt{\rho_0^\ell}\rho^\ell(t)\sqrt{\rho_0^\ell}}\right)^2. \tag{2}$$

It corresponds to the fidelity between initial (ρ_0^ℓ) and time evolved [$\rho^\ell(t)$] reduced density matrices with $\rho^\ell = \mathbf{Tr}_{L-\ell}\rho$, ρ being the total density matrix, ℓ the subsystem size, and L the size of the system. It is known that, in the context of equilibrium quantum phase transitions, the quantum reduced fidelity of a subsystem size as small as two sites characterizes the critical point and exponent [45–48]. The corresponding quantum distance is defined as

$$d_\ell^q(t) = -\frac{1}{\ell}\log\big(F_\ell\big(\rho_0^\ell, \rho^\ell(t)\big)\big), \tag{3}$$

a local observable defined from the quantum reduced fidelity of the subsystem ℓ. Similar to a quasilocal string observable [16] and real-local effective free energy [40], for large L and as $\ell \to L$, the local distance also approaches the rate function $d_\ell^q(t) = \lambda(t)$. Here we show that this quantum reduced fidelity distance exhibits nonanalyticities and obeys scaling laws near the critical point of dQPTs occurring under different quenches in integrable and nonintegrable models.

C. Minimum reduced fidelity distance

The entanglement entropy plays a crucial role in identifying and characterizing dQPTs, and is discussed in Sec. II A. Additionally, the observation that the quantum reduced fidelity is bounded by the fidelity of the associated diagonal states [49] motivates us to develop a distance measure similar to the qRFD, however, utilizing only the eigenvalues of the reduced density matrices.

For instance, if $\eta^\ell_{\uparrow(\downarrow)}$ and $\tau^\ell_{\uparrow(\downarrow)}$ are the eigenvalues of reduced density matrices ρ_0^ℓ and $\rho^\ell(t)$ respectively, then

$$M_\ell(\eta^\ell_\uparrow, \tau^\ell_\downarrow) \leqslant F_\ell\big(\rho_0^\ell, \rho^\ell(t)\big) \leqslant M_\ell(\eta^\ell_\uparrow, \tau^\ell_\uparrow), \tag{4}$$

where $\uparrow / \downarrow$ represent ascending/descending order of the eigenvalues and $M_\ell(\eta^\ell_\uparrow, \tau^\ell_\uparrow) = [\sum_{p=1}^{2^\ell}\sqrt{(\eta^\ell_\uparrow)_p(\tau^\ell_\uparrow)_p}]^2$ is the fidelity between the initial and quenched diagonal states. From the upper bound of the local fidelity, we propose the minimum reduced fidelity distance:

$$d_\ell^m(t) = -\log(M_\ell(\eta^\ell_\uparrow, \tau^\ell_\uparrow)). \tag{5}$$

This distance is an effective measure, as seen in subsequent sections, to study and distinguish the quenches that cause minimal changes in long-range correlations in the system after the quench shown in Figs. 1(a)–1(d) and have avoided crossings in the reduced density matrix spectrum. In the limit $\ell \to L \to \infty$, the eigenvalues of the density matrix are either zero or one, as they represent the occupation of the states. Therefore, in this limit, the mRFD is necessarily zero.

III. RESULTS

In this section, we show that irrespective of the nature of the quench, the qRFD serves as a local measure for dQPT, as observed in both integrable and nonintegrable models. We also explain the category of quenches in which mRFD approximates the critical time and exponent.

A. dQPT in the integrable Ising model

We consider the 1D TFIM with the following Hamiltonian:

$$H = -\sum_{i=1}^{N}\big(\sigma_i^z\sigma_{i+1}^z + h\sigma_i^x\big), \tag{6}$$

where σ's represent the Pauli matrices, h the transverse field strength, and N the size of the spin chain.

The corresponding momentum space Hamiltonian reads

$$H(k) = \vec{d}(k,h)\cdot\vec{\sigma} = 2\sin k\sigma^y + 2(h-\cos k)\sigma^z, \tag{7}$$

with $\vec{d}(k,h) = (0,\ 2\sin k,\ 2(h-\cos k))$ and $\vec{\sigma} = (\sigma^x,\ \sigma^y,\ \sigma^z)$. The equilibrium model shows a quantum phase transition from paramagnetic to ferromagnetic behavior when h changes across the critical point $h_c = 1(-1)$. The quenches across h_c lead to dynamical quantum phase transitions [6,11,50]. The rate function can be obtained in momentum space owing to the translation symmetry of the model,

$$\lambda_k(t) = -\frac{1}{\pi}\mathrm{Re}(\log\int_0^\pi dk\big(|g_k|^2 + \exp^{-2i\epsilon_k^f t}|e_k|^2\big), \tag{8}$$

when the system is quenched from $H_{\text{initial}}(k) = \vec{d}_i(k,h_i)\cdot\vec{\sigma}$ to $H_{\text{final}}(k) = \vec{d}_f(k,h_j)\cdot\vec{\sigma}$ with $|g_k|^2 = \frac{1}{2}[1+\hat{d}_i(k)\cdot\hat{d}_f(k)]$, $|e_k|^2 = \frac{1}{2}[1-\hat{d}_i(k)\cdot\hat{d}_f(k)]$, and $\epsilon_k^f = |\vec{d}_f(k)|$ [14]. The rate function exhibits nonanalyticity at the critical time,

$$t_c = \frac{\pi}{\epsilon_{k^*}^f}\left(n+\frac{1}{2}\right),\quad n = 0,1,2,3,\ldots, \tag{9}$$

where $k^* = \cos^{-1}[\frac{h_ih_f+1}{(h_i+h_f)}]$ is the momentum for which the Loschmidt amplitude vanishes at critical time t_c [6,7,11,14]. The scaling analysis yields the following power-law scaling

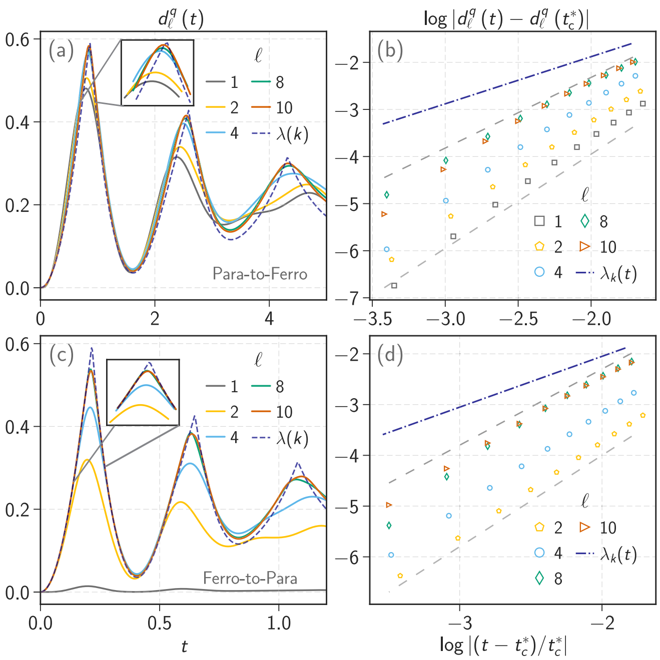

FIG. 2. qRFD for TFIM. (a), (b) Quench I with $h_i = 4$ and $h_f = 0.25$. (c, d) Quench II with $h_i = 0.25$ and $h_f = 4$. (a), (c) qRFD, along with the rate function in momentum space (8). Inset: Magnified area near the first critical point, where the peaks of qRFD approach that of the rate function as the subsystem size ℓ increases. (b), (d) Scaling analysis of qRFD in both quenches. The blue dash dotted line is the scaling of $\lambda_k(t)$ which has a slope equal to 1. The curve fitting of scaling plots of qRFD corresponding to subsystem sizes $\ell = 1$ (or 2 for ferromagnetic-to-paramagnetic quench) and $\ell = 10$ is shown as gray dashed lines. We observe the exponent value to reduce significantly from 1.95(1.85) to 1.53(1.49) as subsystem size increases from $\ell = 2$ to $L/2$ for quench I (quench II). The system size for this calculation is $L = 20$.

close to the transition:

$$\lambda_k(t) - \lambda_k(t_c) \sim \left(\frac{t - t_c}{t_c}\right)^{\nu}, \tag{10}$$

with an exponent $\nu = 1$ in one dimension [10]. In two dimensions the scaling law is logarithmic, $\lambda(t) - \lambda(t_c) \sim (t - t_c)^2 \log|t - t_c|$. See Appendix E for more details on the scaling of the $\lambda(t)$ in the 2D Ising model.

1. *qRFD for quench I and quench II*

The qRFD (3) identifies the critical time and the exponent in dQPT observed under both quenches. The system is initialized in a paramagnetic phase ($|h_i| > 1$) and quenched to ferromagnetic phase ($0 < |h_f| < 1$) in quench I, while quench II is from the ferromagnetic to paramagnetic phase. Considering that the ferromagnetic ground state is degenerate when $h = 0$, all calculations for realizing the ferromagnetic phase are carried out with a nonzero value of h. Additionally, the values of h_i and h_f for which quench I and quench II are realized are considered along the same transition line back and forth, although the results do not explicitly depend on this.

Figures 2(a) and 2(c) show the quantum reduced fidelity distance (3) for different subsystem sizes ℓ for quench I and quench II, respectively. The initial reduced density matrix ρ_0^ℓ and time evolved reduced density matrix $\rho^\ell(t)$ are evaluated exactly. The rate function (8) corresponding to these parameters is shown in Figs. 2(a) and 2(c). The qRFD faithfully approaches the rate function $\lambda(t)$ at the critical time when the subsystem size increases to $\ell \to L/2$, where L is the system size.[1] In this particular quench setup, the postquench correlations are local; therefore, even a subsystem as small as a single spin can also signal the approximate transition time as seen in Fig. 2(a). However, from Fig. 2(c), a minimum of two spins are required to characterize the critical time for quench II, where the quench results in development of long-range correlations.

In Figs. 2(b) and 2(d), the scaling analysis of qRFD and the rate function near the critical point for two quenches is shown. Similar to $\lambda_k(t)$, the qRFD obeys the expected power-law scaling,

$$d_\ell^q(t) - d_\ell^q(t_c^*) \sim \left(\frac{t - t_c^*}{t_c^*}\right)^{\nu},$$

where $\nu \approx 1.95(1.85)$ for $\ell = 2$ and $\nu \approx 1.53(1.49)$ for $\ell = 10$ for paramagnetic to ferromagnetic (ferromagnetic to paramagnetic) quench and t_c^* is the time corresponding to the maximum value (peak) of qRFD corresponding to different subsystem sizes. The t_c^* approaches the critical time, t_c (9) as $\ell \to L/2$. We observe a steady decrease in the exponent value towards the expected Ising universality value $\nu \approx 1$ as the subsystem size ℓ increases towards $L/2$. The observed discrepancy is related to limited access to large system sizes, which we address through mRFD in the next section.

2. *mRFD for quench I*

The mRFD (5) distinguishes and characterizes the dQPT resulting from quench I, which has nearest-neighbor dominated spatial entanglement structure after the quench as seen in Fig. 1. For the integrable model, the initial ($\eta_\uparrow^\ell$) and quenched [$\tau_\uparrow^\ell(t)$] reduced density matrix spectrum and hence the mRFD are calculated from the single-particle correlation matrix [51]. For details of the calculation, refer to Appendix A. Unlike qRFD, this allows us to go to larger system sizes with the following condition $\ell/L << 1$.

We now discuss the evolution of eigenvalues $\tau_\uparrow^\ell(t)$ of reduced density matrix $\rho^\ell(t)$ for quench I as shown in Fig. 3(a). The spectrum exhibits avoided crossings near the critical time of dQPT as shown in the inset in Fig. 3(a). The inset in Fig. 3(b) shows the mRFD (5) calculated from the reduced fidelity between initial and time evolved diagonal states with eigenvalues, $\eta_\uparrow^\ell$ and $\tau_\uparrow^\ell(t)$. The blue dashed lines in the inset represent the critical time calculated using Eq. (9). With increasing subsystem sizes ℓ, the time t_c^* at which the mRFD peaks approaches the critical time, t_c. Nonetheless, we observe deviation from the exact critical time in the avoided crossings (critical time) in the reduced density matrix spectrum

[1]Though the subsystem size is taken to be simply connected in all the data shown in the main text, the qRFD averaged over a few combinations of random partitions also identifies the transition times as shown in Appendix B.

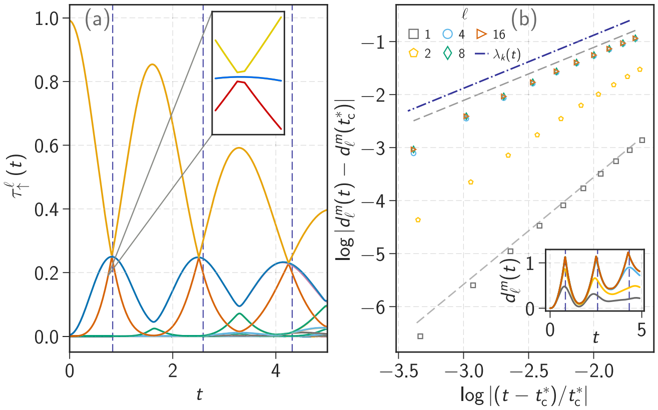

FIG. 3. mRFD for TFIM. (a) Reduced density matrix spectrum of $\rho^\ell(t)$, corresponding to quench I with $h_i = 4$, $h_f = 0.25$ and $\ell = 8$, $L = 64$. The blue dashed lines represent the critical times. Close to the critical times, the spectrum exhibits avoided crossing as shown in the inset. The inset in (b) is the mRFD for the same quench parameters. The dashed lines correspond to the critical time calculated using Eq. (9). (b) Scaling analysis of mRFD near the first critical point. The slope varies between 2.02 for $\ell = 1$ to 1.02 for $\ell = 8, 16$. The gray lines represent the curve fitting corresponding to $\ell = 1$ and 2. The blue dash dotted line represents the scaling of the rate function.

(mRFD) as seen in Figs. 3(a) and 3(b). However, it vanishes for quench I with $h_i = 4$ and $h_f = 0$, where the return amplitude peaks do not decay and the avoided crossings in the reduced density and mRFD show nonanalyticity precisely at the critical time calculated using Eq. (9). Such discrepancies, appearing as deviations in the critical time of local observables from that of the rate function, are also observed in Ref. [37] for topological models under quenches with oscillatory degeneracies in the entanglement spectrum. This is believed to be attributed to the distinctive characteristics of the propagation of the mutual information or entanglement between different parts of the subsystem as time evolves.

The scaling analysis of mRFD near the time t_c^* at which it peaks gives

$$d_\ell^m(t) - d_\ell^m(t_c^*) \sim \left(\frac{t - t_c^*}{t_c^*}\right)^\nu,$$

with the critical exponent $\nu \approx 1$ for $\ell = 8$ and 16, which is what one would expected and as seen in the rate function Fig. 3(b). Hence, though mRFD is a finite-size observable, for quench I in TFIM, it serves as an efficient local quantity that reproduces the scaling and universality of dQPT. For quench II, where the change in long-range correlations is significant, the information in diagonal states is insufficient to understand the dQPT fully. Like entanglement entropy, the mRFD exhibits linear growth near the critical time for quench II.

Here we considered the dQPT observed during quenches across the equilibrium critical point in 1D TFIM. The efficiency of qRFD and mRFD in more general scenarios, such as understanding anomalous dQPTs, where the quenches are done within the same equilibrium phase, and the 2D Ising model is discussed in Appendixes D and E respectively.

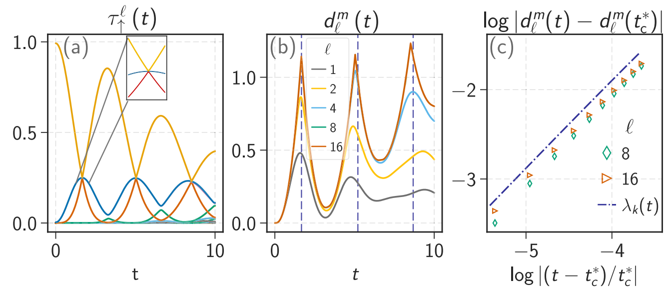

FIG. 4. mRFD for the topological model. (a, b) Reduced density matrix spectrum and mRFD calculated for quench I. The inset in (a) shows the avoided level crossing near the critical time. The spectrum is for $\ell = 8$ and $L = 64$. The scaling analysis of mRFD gives a critical exponent $\nu \approx 0.96$ for $\ell = 8$ and similarly for $\ell = 16$. The blue dash dotted line in (c) represents the scaling of return amplitude calculated in momentum space.

3. mRFD and topological dQPT

The fermionic momentum space Hamiltonian in Eq. (7) has a well-defined topology. The topological order parameter, winding number $\nu_D = \frac{1}{2\pi i}\int_{-\pi}^{\pi} dk \frac{d}{dk}\log[h(k)]$, where $h(k) = d_x(k) - i d_y(k)$, identifies the trivial and topological phases [52]. Quench I in the spin chain (6) corresponds to a quench from the trivial ($\nu_D = 0$) to topological phase ($\nu_D = 1$) in the momentum space Hamiltonian. Under this quench, the correlations are local while the presence of edge states in the initial phase contributes to long-range correlations for quench II [35]. Hence, the mRFD is a useful measure for detecting the occurrence of a topological dQPT in fermionic models under quench I.

Figures 4(a)–4(c) show the quenched reduced density matrix spectrum, mRFD, and its scaling for the topological chiral symmetric fermionic model under quench I. Appendix C includes a detailed description of the model and the efficiency of qRFD in capturing the critical time and exponent of dQPT resulting from quench I and quench II. In the vicinity of the critical point of quench I, avoided crossings and sharp kinks are seen in the quenched reduced density matrix spectrum and the mRFD, respectively. The mRFD displays much faster convergence to the expected power-law scaling with an exponent $\nu \approx 0.96$ for $\ell = 8$ compared to qRFD.

B. dQPT in the nonintegrable model

We consider the following transverse axial next-nearest-neighbor Ising model:

$$H = -\sum_{i=1}^{N} h\sigma_i^x + \sigma_i^z\sigma_{i+1}^z + \Delta\sigma_i^z\sigma_{i+2}^z. \tag{11}$$

In the $\Delta = 0$ limit, the model assumes the same form as TFIM (6) and can be solved analytically. However, for $\Delta \neq 0$, the Jordan-Wigner transformation translates the model to an interacting fermionic chain which does not allow an exact solution. Depending on the strength of this integrability breaking interaction, Δ and the transverse field strength h, the equilibrium model exhibits four distinct phases: paramagnetic, ferromagnetic, floating phase, and an antiphase [50,53]. The dQPT arises when any or both parameters, Δ and h, are

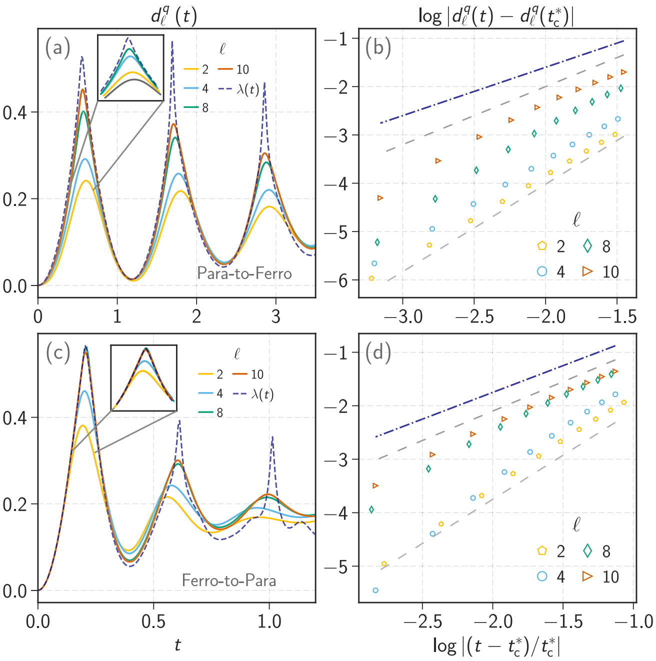

FIG. 5. qRFD for the nonintegrable model. (a), (c) qRFD (3) for different subsystem sizes and the real-space rate function (1). The quench parameters are $h_i = 2(0)$, $\Delta_i = 0.5(0)$, $h_f = 0.5(4)$, $\Delta_f = 0.5(0.6)$ for quench I (quench II). (b), (d) Scaling analysis of qRFD near the time at which the first peak appears. The slope of the curve varies from 1.75(1.65) for $\ell = 2$ to 1.20(1.10) for $\ell = 10$ for quench I (quench II). The blue dash dotted lines are reference curves with the slope 1 and the gray dashed lines represent the curve fitting corresponding to subsystem sizes $\ell = 2$ and 10. The system size is $L = 20$.

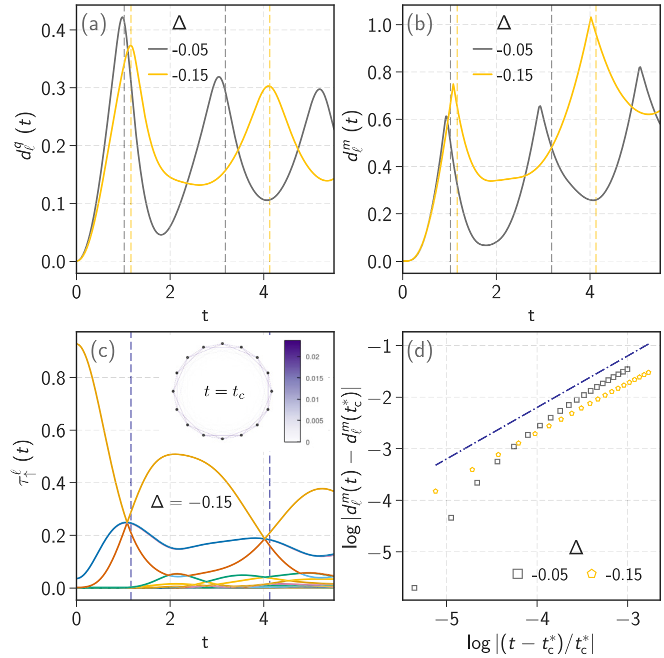

FIG. 6. (a), (b) mRFD for the nonintegrable model showing the qRFD (3) and the mRFD (5) for quench I for different Δ, $h_i = 1.3$, $h_f = 0.2$, $\ell = 10$, and $L = 20$. The nonanalyticities of mRFD display a shift compared to the transition time of qRFD, and it depends on Δ. (c) The reduced density matrix spectrum for the quenched state corresponding to $\Delta = -0.15$. Inset: Change in mutual information after the quench. (d) Scaling analysis for the mRFD for $\Delta = -0.05, -0.15$. For $\Delta = -0.05$ the slope is 1.17 and for $\Delta = -0.15$ it is 0.95 for subsystem size $\ell = 10$. The blue dash dotted line indicates a slope of 1.

quenched across an equilibrium critical point [16,50]. It is observed that the increase in the absolute value of Δ, the integrability breaking term, along the positive (negative) direction manifests as a decrease (increase) in the critical time scale. Unlike the critical time, t_c (9) of the TFIM, there is nonequal spacing of t_c when $\Delta \neq 0$ [50].

1. qRFD for quench I and quench II

We follow a similar philosophy as in the previous section to choose parameters such that they represent the quench I and quench II protocols and show dQPT. Instead of momentum space, here, we calculate all the density matrices directly in the real space. This severely limits the accessible system sizes in exact diagonalization calculations.

Figures 5(a) and 5(c) show the quantum reduced fidelity distance (3) along with the rate function for quench I and quench II. As the subsystem size, ℓ, increases, the time t_c^* at which the qRFD peaks approaches the critical point at which the rate function shows nonanalyticities in time. The scaling analysis of qRFD near the first critical point, shown in Figs. 5(b) and 5(d), indicates a similar scaling law; the qRFD follows a power-law scaling, $d_\ell^q(t) - d_\ell^q(t_c^*) \sim [(t - t_c^*)/t_c^*]^\nu$, with $\nu \approx 1.75(1.65)$ for $l = 2$ and $\nu \approx 1.20(1.10)$ for $\ell = 10$ for quench I (quench II). The blue dotted line in Figs. 5(b) and 5(d) is the curve that has a power-law behavior with exponent 1.

For this particular model, [16] showed that for a chain with $L = 16$ spins and a local string size ranging as $10 \leqslant \ell \leqslant L$, the quasilocal observable exhibits power-law scaling with an exponent $\nu \approx 1$. Similarly, as the subsystem size ℓ increases, the critical exponent of qRFD of the nonintegrable model gradually approaches that of the qRFD of the integrable model, but with visible finite-size effects.

2. mRFD for quench I

Figures 6(a) and 6(b) are the qRFD and mRFD corresponding to quench I with varying Δ ($\Delta_i = \Delta_f = \Delta$), with dotted lines representing critical time obtained from the rate function. The critical time scale of qRFD and mRFD increases upon increasing the strength of the integrability breaking term, Δ. No simple quantitative relation exists for t_c like in Eq. (9) for the 1D TFIM, and the dQPT appears at unequal time intervals. Similar to the integrable case, the transition time of the quench I dQPT in mRFD experiences a shift dependent on Δ relative to the critical time of the rate function or qRFD. Figure 6(c) shows the reduced density matrix spectrum with avoided crossing near the critical time. The inset in Fig. 6(c) reveals that, even in the presence of integrability breaking terms, the mRFD identifies and distinguishes quench I, scenarios where postquench changes in quantum correlations are local. Figure 6(d) shows the scaling analysis of mRFD for different Δ's. The mRFD obeys the power-law scaling, $d_\ell^m(t) -$

$d_\ell^m(t_c^*) \sim [(t - t_c^*)/t_c^*]^\nu$, with $\nu \approx 1.17$ for $\Delta = -0.05$ to $\nu \approx 0.95$ for $\Delta = -0.15$.

IV. CONCLUSION

In this paper, we have demonstrated the efficacy of the quantum reduced fidelity distance as a local observable for understanding the dQPT that occurs in diverse models, including integrable and nonintegrable spin chains and topological systems. The quantum distance metric is defined based on the reduced fidelity between the initial and quenched states for finite subsystems. Notably, as the subsystem size ($\ell \sim L/2$) increases, the critical time and the critical exponents identified by the qRFD gradually converge to the point where the rate function exhibits nonanalytic behavior.

Moreover, the local observable derived from the diagonal states, with minimum reduced fidelity distance, distinguishes dQPTs arising from different quenches. The rationale for introducing mRFD comes from the observation that for a specific quench protocol (quench I), the entanglement spectrum features avoided level crossings near the transition time during the time evolution. Additionally, the quantum correlations developed after quench I remain local. Another key insight is that irrespective of the nature of the quench, the fidelity between diagonal states or eigenvalue distributions sets an upper limit on the quantum reduced fidelity. These findings underscore the importance of local observables, particularly mRFD, in effectively probing and characterizing the diverse dynamical phases that arise during quantum quench processes.

While the qRFD and mRFD have proven valuable in comprehending dQPT by exhibiting cusps at critical times, some areas will benefit from further improvements. First, due to limited access to large system sizes, the critical exponent, ν, obtained from the scaling analysis of qRFD does not precisely match with the expected exponent $\nu \simeq 1$. However, the relative error in calculating the exponent, $\delta\nu = \nu - 1$, decreases from 0.95 to 0.53 (0.75 to 0.20) upon increasing the subsystem size from $\ell = 2$ to $L/2$ for the integrable (nonintegrable) spin model. The finite-size effects observed for the nonintegrable model are less compared to the integrable model. It is interesting to note that similar finite-size effects are also observed in the real-space local effective free energy proposed by Halimeh *et al.* [40]. Though the critical time is reliably found from the effective free energy corresponding to subsystem size as small as $\ell = 2$, the nonanalytic behavior becomes more evident as the subsystem size increases to $\ell \geqslant 32$. In this respect, mRFD effectively addresses the finite-size effects in integrable models by calculating the eigenvalues of the reduced density matrix from the single-particle correlation matrix, enabling access to large system sizes. For instance, we successfully identified the critical time and precise critical exponent for a subsystem size of $\ell = 8$ for $L = 64$.

Finally, note that with the emergence of techniques capable of measuring reduced density matrices, the qRFD and mRFD can serve as convenient methods for experimentally detecting dQPTs [54–56]. For instance, the local projective measurements were performed on a subset of Bose-Einstein condensates of ^{87}Rb atoms in an optical lattice [57] and the investigation of the propagation of nonlocal correlations in the trapped $^{171}\mathrm{Yb}^+$ ions [58] provides information about the subsystem density matrix at finite time and thus exemplifies the practical applicability of the qRFD and mRFD.

ACKNOWLEDGMENTS

We would like to thank Himadri S. Dhar for an earlier collaboration on a closely related project, and several useful discussion. We thank Markus Heyl for a critical reading of the paper. We also gratefully acknowledge the valuable discussions with the late Amit Dutta during this reserach. S.B. would like to thank MPG for funding through the Max Planck Partner Group at IITB. R.V.B. would like to thank DST-INSPIRE fellowship (Grant No. IF180067) for funding. We used the open-source QUSPIN package [59,60] for exact diagonalization calculation.

APPENDIX A: REDUCED DENSITY MATRIX SPECTRUM FROM A TWO-POINT CORRELATION FUNCTION FOR AN INTEGRABLE MODEL

The initial ground state of Eq. (7) at $h_i = 4$,

$$|\psi_k\rangle = u_k c_k^\dagger c_{-k}^\dagger |0\rangle + v_k |0\rangle , \tag{A1}$$

is used to calculate the one-body correlation matrix,

$$\mathbf{C}_{\text{initial}} = \begin{pmatrix} \mathbb{C} & \mathbb{F} \\ \mathbb{F}^\dagger & \mathbb{I} - \mathbb{C} \end{pmatrix},$$

where

$$\mathbb{C}_{ij} = \langle c_i^\dagger c_j \rangle = \frac{2}{L} \sum_{k \in BZ/2} |u_k|^2 \cos(k(i-j)),$$

$$\mathbb{F}_{ij} = \langle c_i^\dagger c_j^\dagger \rangle = \frac{2}{L} \sum_{k \in BZ/2} u_k^* v_k \sin(k(i-j)), \tag{A2}$$

and i and j run over the subsystem size ℓ. The entanglement spectrum (ϵ) is calculated from the eigenvalues of the correlation matrix (ζ),

$$\zeta_q^\ell = \frac{1}{e^{\epsilon_q^\ell} + 1},$$

where $q \in 0, 1, \dots, \ell$. The 2^ℓ eigenvalue of the initial reduced density matrix (ρ_0^ℓ) is then obtained from the entanglement spectrum as [61]

$$\eta_p^\ell = \frac{1}{\mathcal{Z}} \Pi_q e^{-\epsilon_q^\ell n_q^{(p)}},$$

where $n_q^{(p)} \in 0, 1$ are single level occupation numbers. $\mathcal{Z}$ is the normalization constant such that $\sum_p \eta_p^\ell = 1$. To observe dQPT, the ground state (A1) is time evolved with respect to the Hamiltonian (7) at $h_f = 0.25$. At any instant of time, the quenched state is $|\psi_k(t)\rangle = u_k(t) c_k^\dagger c_{-k}^\dagger |0\rangle + v_k(t)|0\rangle$. From these time-dependent coefficients, the correlation matrix [$\mathbb{C}(t)$], and hence the quenched reduced density matrix spectrum with eigenvalues arranged in ascending order, $\tau_\uparrow^\ell(t)$ is calculated using the same procedure described above.

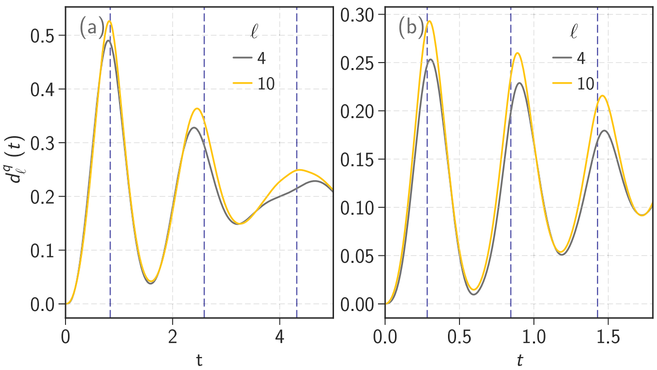

FIG. 7. qRFD for random partitions. (a), (b) qRFD averaged over ten random partitions of size $\ell = 4, 10$ for integrable and nonintegrable spin chains. The quench parameters chosen for integrable (6) and nonintegrable (11) models are $h_i = 4.0$, $h_f = 0.25$ and $h_i = 2$, $h - f = 0.5$, $\Delta_i = \Delta_f = 0.5$ respectively. The blue dashed lines represent the critical time. As ℓ increases, the qRFD approaches the critical time.

APPENDIX B: QRFD FOR RANDOM PARTITIONS

Here we show the qRFD calculated for dQPT observed in both integrable (6) and nonintegrable (11) spin chains when the choice of subsystem sites is random. Consider the paramagnetic to ferromagnetic quench discussed in Secs. III A 1 and III B 1. We consider ten configurations of random subsystem sites of size $\ell = 4, 10$ for $L = 20$. The qRFD (3) values averaged over these random configurations for the integrable and nonintegrable models are plotted in Figs. 7(a) and 7(b), respectively. The blue dotted lines represent the critical time. As the subsystem size increases, the qRFD averaged over random partitions approaches the critical time. For the opposite quench also, qRFD averaged over random partitions picks up the critical time efficiently.

APPENDIX C: FERMIONIC TOPOLOGICAL MODEL

We consider the chiral symmetric Hamiltonian in class AIII of topological insulators and superconductors [62],

$$H = \sum_{i=1}^{N} \left(\frac{1}{2} c_i^\dagger (\sigma^x + i\sigma^y) c_{i+1} + \text{H.c.}\right) + \sum_{i=1}^{N} m c_i^\dagger \sigma^y c_i, \quad \text{(C1)}$$

where $c_i^\dagger (c_i)$ are the fermion creation (annihilation) operators, σ's are the Pauli matrices, m is the complex dimerization amplitude, and N is the number of unit cells. In the Fourier space,

$$H(k) = d(\vec{k}) \cdot \vec{\sigma} = \cos k \sigma^x + (m - \sin k)\sigma^y, \quad \text{(C2)}$$

where $d(\vec{k}) = (\cos k, (m - \sin k), 0)$ and $\vec{\sigma} = (\sigma^x, \sigma^y, \sigma^z)$. In equilibrium, the model has a nontrivial topological index for $0 < m < 1$ and a trivial topological index for $m > 1$. Quenching the parameter m across the equilibrium critical point $m_c = 1$ results in dynamical quantum phase transitions. By changing $m_i = 0.25(4)$ to $m_f = 4(0.25)$, we get topological (trivial) to trivial (topological) quench.

Figures 8(a) and 8(b) correspond to the qRFD (3) calculated for both quenches for different subsystem sizes. The

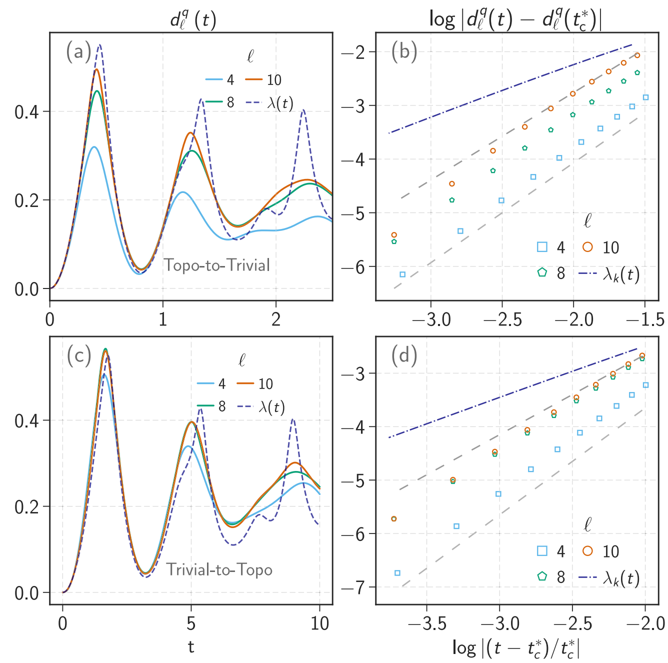

FIG. 8. qRFD for the topological model. (a), (c) qRFD calculated for different subsystem sites for quench I and quench II. It also has the rate function calculated in real space. The total number of sites is $L = 20$. The quench parameters are $m_i = 0.25$, $m_f = 4.0$ (a) and $m_i = 4$, $m_f = 0.25$ (c). (b), (d) Scaling analysis of qRFD for both quenches. The slope of the curve changes from 1.86(1.98) for $\ell = 4$ to 1.63(1.74) for $\ell = 10$ during quench II (quench I). The blue dash dotted line in (b) and (d) is the slope 1 curve.

rate function calculated in real space is also plotted for both quenches. The qRFD captures the critical point efficiently. The scaling analysis of both quenches shows a power-law behavior, with the critical exponent $\nu \approx 1.86(1.98)$ for $l = 4$ to $\nu = 1.63(1.74)$ for $l = 10$ for topological to trivial (trivial to topological) quench. The mRFD and its scaling for the quench from the trivial to the topological phase where only local correlations are present [35] are explained in Sec. III A 3.

APPENDIX D: QRFD IN ANOMALOUS dQPT

When the quench parameters do not cross the equilibrium quantum critical point, we get the anomalous dQPT [31]. The spin Hamiltonian,

$$H = \sum_{i=1}^{N} -h\sigma_i^z + J_x \sigma_i^x \sigma_{i+1}^x + J_y \sigma_i^y \sigma_{i+1}^y, \quad \text{(D1)}$$

exhibits anomalous dQPT. Since this is an integrable model, the diagonalization in momentum space is possible with

$$H(k) = \vec{d}(k, h) \cdot \vec{\sigma} = 2\gamma \sin k \sigma^y + 2(h - \cos k)\sigma^z, \quad \text{(D2)}$$

where $\vec{d}(k, h) = (0,\ 2\gamma \sin k,\ 2(h - \cos k))$, $\vec{\sigma} = (\sigma^x, \sigma^y, \sigma^z)$ are the Pauli matrices, $J_x = (1 + \gamma)/2$, and $J_y = (1 - \gamma)/2$. Consider the quench, $\gamma_i = 1.6$, $h_i = 1.5$ to $\gamma_f = -4$, $h_f = 3$, which is within the paramagnetic phase [31]. Figure 9(a) corresponds to the qRFD (3) for different subsystem sizes. The return amplitude is calculated in the

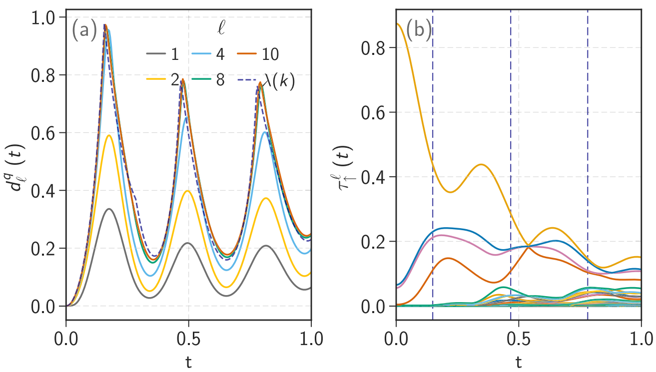

FIG. 9. qRFD for anomalous dQPT. (a) qRFD for different subsystem sizes and the rate function. The quench performed is from $\gamma_i = 1.6,\ h_i = 1.5$ to $\gamma_f = -4,\ h_f = 3$. The total system size is $L = 20$. (b) Reduced density matrix spectrum calculated from the single-particle correlation matrix for the same quench. The subsystem size is $\ell = 8$, and the total system size is $L = 64$. The blue dashed lines indicate the critical time at which the rate function diverges.

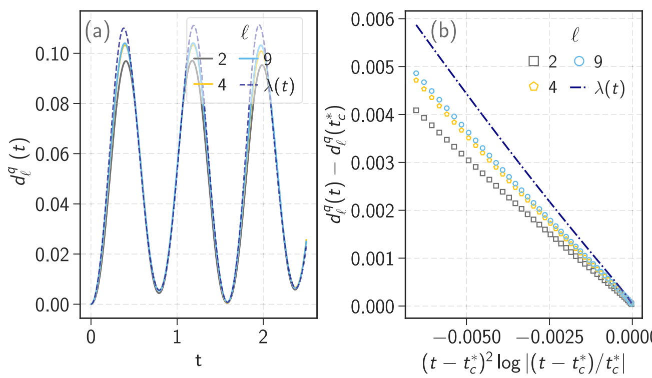

FIG. 10. qRFD for 2D TFIM. (a) qRFD for different subsystem sizes and $\lambda(t)$ calculated in real space for a 4×4 square lattice. The system is quenched from $h_i = 1.5J$ to $h_f = 0.25J$ for $J = J_p = 1$. The subsystem size chosen is $\ell = 2$ sites and areas with size $\ell = 4(2 \times 2)$ and $9(3 \times 3)$. (b) Scaling analysis of qRFD for different subsystem sizes. As the subsystem size increases, the qRFD also shows similar logarithmic scaling as $\lambda(t)$.

momentum space using Eq. (8). As the subsystem size increases, the maximum value of qRFD moves towards the peak value of the rate function, thus identifying the critical time efficiently.

The reduced density matrix spectrum calculated using the single-particle correlation matrix, as explained in Appendix A, is shown in Fig. 9(b). Though the spectrum shows a single avoided crossing at some time, it lies much away from the critical time indicated by the blue dotted line and does not show oscillations like Fig. 3(a). Hence the mRFD fails to capture the anomalous dQPT.

APPENDIX E: QRFD IN TFIM ON A SQUARE LATTICE

Consider the TFIM (6) on a square lattice,

$$H = -\sum_{\langle ij \rangle} J_{ij} \sigma_i^z \sigma_j^z - h \sum_{i=1}^{L} \sigma_i^x, \tag{E1}$$

where the nearest-neighbor hopping takes value $J_{ij} = J$ along the rows and $J_{ij} = J_p$ along the columns, and L is the total number of lattice sites. During the quench from $h_i = 1.5J$ to $h_f = 0.25J$ and for $J = J_p = 1$, the model undergoes dynamical quantum phase transition. Near the critical point, the rate function obeys the following scaling relation [10]:

$$\lambda(t) - \lambda(t_c) \sim (t - t_c)^2 \log |t - t_c|, \tag{E2}$$

where t_c is the critical time. The quantum fidelity distance for different choices of subsystem size, along with the rate function, is shown in Fig. 10(a). The critical point is identified well by the local quantum distance. Figure 10(b) shows that similar to the scaling of $\lambda(t)$ (E2), the qRFD also exhibits logarithmic scaling:

$$d_\ell^q(t) - d_\ell^q(t_c^*) \sim (t - t_c^*)^2 \log |t - t_c^*|. \tag{E3}$$

The reduced density matrix spectrum does not show avoided crossings at the critical time for this quench. Hence, the minimum reduced fidelity distance (5) is not a reliable local measure. The quench at which mRFD can capture dQPT in this model needs to be studied further.

[1] H. E. Stanley, Scaling, universality, and renormalization: Three pillars of modern critical phenomena, Rev. Mod. Phys. **71**, S358 (1999).

[2] L. P. Kadanoff, W. Götze, D. Hamblen, R. Hecht, E. A. S. Lewis, V. V. Palciauskas, M. Rayl, J. Swift, D. Aspnes, and J. Kane, Static phenomena near critical points: Theory and experiment, Rev. Mod. Phys. **39**, 395 (1967).

[3] S. Ryu, A. P. Schnyder, A. Furusaki, and A. W. W. Ludwig, Topological insulators and superconductors: tenfold way and dimensional hierarchy, New J. Phys. **12**, 065010 (2010).

[4] A. Kitaev, V. Lebedev, and M. Feigel'man, Periodic table for topological insulators and superconductors, *Advances in Theoretical Physics: Landau Memorial Conference*, AIP Conf. Proc. No. 1134 (AIP, New York, 2009), pp. 22–30.

[5] A. P. Schnyder, S. Ryu, A. Furusaki, and A. W. W. Ludwig, Classification of topological insulators and superconductors in three spatial dimensions, Phys. Rev. B **78**, 195125 (2008).

[6] M. Heyl, Dynamical quantum phase transitions: A review, Rep. Prog. Phys. **81**, 054001 (2018).

[7] M. Heyl, Dynamical quantum phase transitions: A brief survey, Europhys. Lett. **125**, 26001 (2019).

[8] B. Mera, C. Vlachou, N. Paunković, V. R. Vieira, and O. Viyuela, Dynamical phase transitions at finite temperature from fidelity and interferometric Loschmidt echo induced metrics, Phys. Rev. B **97**, 094110 (2018).

[9] H. Lang, Y. Chen, Q. Hong, and H. Fan, Dynamical quantum phase transition for mixed states in open systems, Phys. Rev. B **98**, 134310 (2018).

[10] M. Heyl, Scaling and universality at dynamical quantum phase transitions, Phys. Rev. Lett. **115**, 140602 (2015).

[11] M. Heyl, A. Polkovnikov, and S. Kehrein, Dynamical quantum phase transitions in the transverse-field Ising model, Phys. Rev. Lett. **110**, 135704 (2013).
[12] S. Sharma, U. Divakaran, A. Polkovnikov, and A. Dutta, Slow quenches in a quantum Ising chain: Dynamical phase transitions and topology, Phys. Rev. B **93**, 144306 (2016).
[13] I. Hagymási, C. Hubig, O. Legeza, and U. Schollwöck, Dynamical topological quantum phase transitions in nonintegrable models, Phys. Rev. Lett. **122**, 250601 (2019).
[14] J. C. Budich and M. Heyl, Dynamical topological order parameters far from equilibrium, Phys. Rev. B **93**, 085416 (2016).
[15] A. Lahiri and S. Bera, Dynamical quantum phase transitions in weyl semimetals, Phys. Rev. B **99**, 174311 (2019).
[16] S. Bandyopadhyay, A. Polkovnikov, and A. Dutta, Observing dynamical quantum phase transitions through quasilocal string operators, Phys. Rev. Lett. **126**, 200602 (2021).
[17] M. Sadrzadeh, R. Jafari, and A. Langari, Dynamical topological quantum phase transitions at criticality, Phys. Rev. B **103**, 144305 (2021).
[18] L. Rossi and F. Dolcini, Nonlinear current and dynamical quantum phase transitions in the flux-quenched Su-Schrieffer-Heeger model, Phys. Rev. B **106**, 045410 (2022).
[19] K. Sim, R. Chitra, and P. Molignini, Quench dynamics and scaling laws in topological nodal loop semimetals, Phys. Rev. B **106**, 224302 (2022).
[20] R. Okugawa, H. Oshiyama, and M. Ohzeki, Mirror-symmetry-protected dynamical quantum phase transitions in topological crystalline insulators, Phys. Rev. Res. **3**, 043064 (2021).
[21] V. Vijayan, L. Chotorlishvili, A. Ernst, S. S. P. Parkin, M. I. Katsnelson, and S. K. Mishra, Topological dynamical quantum phase transition in a quantum skyrmion phase, Phys. Rev. B **107**, L100419 (2023).
[22] L. Zhang, W. Jia, and X.-J. Liu, Universal topological quench dynamics for Z2 topological phases, Sci. Bull. **67**, 1236 (2022).
[23] W. Jia, L. Zhang, L. Zhang, and X.-J. Liu, Dynamical detection of mean-field topological phases in an interacting chern insulator, Phys. Rev. B **107**, 125132 (2023).
[24] S. Bandyopadhyay, S. Bhattacharjee, and D. Sen, Driven quantum many-body systems and out-of-equilibrium topology, J. Phys.: Condens. Matter **33**, 393001 (2021).
[25] W. C. Yu, P. D. Sacramento, Y. C. Li, and H.-Q. Lin, Correlations and dynamical quantum phase transitions in an interacting topological insulator, Phys. Rev. B **104**, 085104 (2021).
[26] S. Vajna and B. Dóra, Topological classification of dynamical phase transitions, Phys. Rev. B **91**, 155127 (2015).
[27] Z. Huang and A. V. Balatsky, Dynamical quantum phase transitions: Role of topological nodes in wave function overlaps, Phys. Rev. Lett. **117**, 086802 (2016).
[28] R. Jafari, Dynamical quantum phase transition and quasi particle excitation, Sci. Rep. **9**, 2871 (2019).
[29] B. Žunkovič, M. Heyl, M. Knap, and A. Silva, Dynamical quantum phase transitions in spin chains with long-range interactions: Merging different concepts of nonequilibrium criticality, Phys. Rev. Lett. **120**, 130601 (2018).
[30] J. C. Halimeh and V. Zauner-Stauber, Dynamical phase diagram of quantum spin chains with long-range interactions, Phys. Rev. B **96**, 134427 (2017).
[31] S. Vajna and B. Dóra, Disentangling dynamical phase transitions from equilibrium phase transitions, Phys. Rev. B **89**, 161105(R) (2014).
[32] S. Porta, F. Cavaliere, M. Sassetti, and N. Traverso Ziani, Topological classification of dynamical quantum phase transitions in the XY chain, Sci. Rep. **10**, 12766 (2020).
[33] E. Canovi, P. Werner, and M. Eckstein, First-order dynamical phase transitions, Phys. Rev. Lett. **113**, 265702 (2014).
[34] S. De Nicola, A. A. Michailidis, and M. Serbyn, Entanglement view of dynamical quantum phase transitions, Phys. Rev. Lett. **126**, 040602 (2021).
[35] N. Sedlmayr, P. Jaeger, M. Maiti, and J. Sirker, Bulk-boundary correspondence for dynamical phase transitions in one-dimensional topological insulators and superconductors, Phys. Rev. B **97**, 064304 (2018).
[36] Z. Gong and M. Ueda, Topological entanglement-spectrum crossing in quench dynamics, Phys. Rev. Lett. **121**, 250601 (2018).
[37] K. Pöyhönen and T. Ojanen, Entanglement echo and dynamical entanglement transitions, Phys. Rev. Res. **3**, L042027 (2021).
[38] R. Jafari and A. Akbari, Floquet dynamical phase transition and entanglement spectrum, Phys. Rev. A **103**, 012204 (2021).
[39] P. Jurcevic, H. Shen, P. Hauke, C. Maier, T. Brydges, C. Hempel, B. P. Lanyon, M. Heyl, R. Blatt, and C. F. Roos, Direct observation of dynamical quantum phase transitions in an interacting many-body system, Phys. Rev. Lett. **119**, 080501 (2017).
[40] J. C. Halimeh, D. Trapin, M. Van Damme, and M. Heyl, Local measures of dynamical quantum phase transitions, Phys. Rev. B **104**, 075130 (2021).
[41] S. Bandyopadhyay, A. Polkovnikov, and A. Dutta, Late-time critical behavior of local stringlike observables under quantum quenches, Phys. Rev. B **107**, 064105 (2023).
[42] L. Amico, R. Fazio, A. Osterloh, and V. Vedral, Entanglement in many-body systems, Rev. Mod. Phys. **80**, 517 (2008).
[43] S.-J. Gu, Fidelity approach to quantum phase transitions, Int. J. Mod. Phys. B **24**, 4371 (2010).
[44] D. F. Abasto, A. Hamma, and P. Zanardi, Fidelity analysis of topological quantum phase transitions, Phys. Rev. A **78**, 010301(R) (2008).
[45] M. Jian, X. Lei, and W. Xiao-Guang, Reduced fidelity susceptibility in one-dimensional transverse field Ising model, Commun. Theor. Phys. **53**, 175 (2010).
[46] E. Eriksson and H. Johannesson, Reduced fidelity in topological quantum phase transitions, Phys. Rev. A **79**, 060301(R) (2009).
[47] W.-L. You and W.-L. Lu, Scaling of reduced fidelity susceptibility in the one-dimensional transverse-field XY model, Phys. Lett. A **373**, 1444 (2009).
[48] J. Ma, L. Xu, H.-N. Xiong, and X. Wang, Reduced fidelity susceptibility and its finite-size scaling behaviors in the Lipkin-Meshkov-Glick model, Phys. Rev. E **78**, 051126 (2008).
[49] D. Markham, J. A. Miszczak, Z. Puchała, and K. Życzkowski, Quantum state discrimination: A geometric approach, Phys. Rev. A **77**, 042111 (2008).
[50] C. Karrasch and D. Schuricht, Dynamical phase transitions after quenches in nonintegrable models, Phys. Rev. B **87**, 195104 (2013).
[51] M.-C. Chung and I. Peschel, Density-matrix spectra of solvable fermionic systems, Phys. Rev. B **64**, 064412 (2001).
[52] J. K. Asbóth, L. Oroszlány, and A. Pályi, *A Short Course on Topological Insulators* (Springer, New York, 2016).
[53] W. Selke, The ANNNI model theoretical analysis and experimental application, Phys. Rep. **170**, 213 (1988).

[54] T. Xin, D. Lu, J. Klassen, N. Yu, Z. Ji, J. Chen, X. Ma, G. Long, B. Zeng, and R. Laflamme, Quantum state tomography via reduced density matrices, Phys. Rev. Lett. **118**, 020401 (2017).
[55] N. Paunković, P. D. Sacramento, P. Nogueira, V. R. Vieira, and V. K. Dugaev, Fidelity between partial states as a signature of quantum phase transitions, Phys. Rev. A **77**, 052302 (2008).
[56] C. Kokail, R. van Bijnen, A. Elben, B. Vermersch, and P. Zoller, Entanglement Hamiltonian tomography in quantum simulation, Nat. Phys. **17**, 936 (2021).
[57] A. M. Kaufman, M. E. Tai, A. Lukin, M. Rispoli, R. Schittko, P. M. Preiss, and M. Greiner, Quantum thermalization through entanglement in an isolated many-body system, Science **353**, 794 (2016).
[58] P. Richerme, Z.-X. Gong, A. Lee, C. Senko, J. Smith, M. Foss-Feig, S. Michalakis, A. V. Gorshkov, and C. Monroe, Non-local propagation of correlations in quantum systems with long-range interactions, Nature (London) **511**, 198 (2014).
[59] P. Weinberg and M. Bukov, QuSpin: A Python package for dynamics and exact diagonalisation of quantum many body systems part I: Spin chains, SciPost Phys. **2**, 003 (2017).
[60] P. Weinberg and M. Bukov, QuSpin: A Python package for dynamics and exact diagonalisation of quantum many body systems. Part II: Bosons, fermions and higher spins, SciPost Phys. **7**, 020 (2019).
[61] J. Sirker, M. Maiti, N. P. Konstantinidis, and N. Sedlmayr, Boundary fidelity and entanglement in the symmetry protected topological phase of the SSH model, J. Stat. Mech.: Theory Exp. (2014) P10032.
[62] I. Mondragon-Shem, T. L. Hughes, J. Song, and E. Prodan, Topological criticality in the chiral-symmetric aiii class at strong disorder, Phys. Rev. Lett. **113**, 046802 (2014).